A comprehensive analysis of the Illapel 2015 Mw 8.3 Earthquake from GPS and InSAR data.

Klein, E.[1][2], Vigny, C.[1], Fleitout, L.[1], Grandin, R.[3], Jolivet, R.[1], Rivera, E.[4], Métois, M.[5]

Supplementary material

GPS Data

High rate GPS data processing

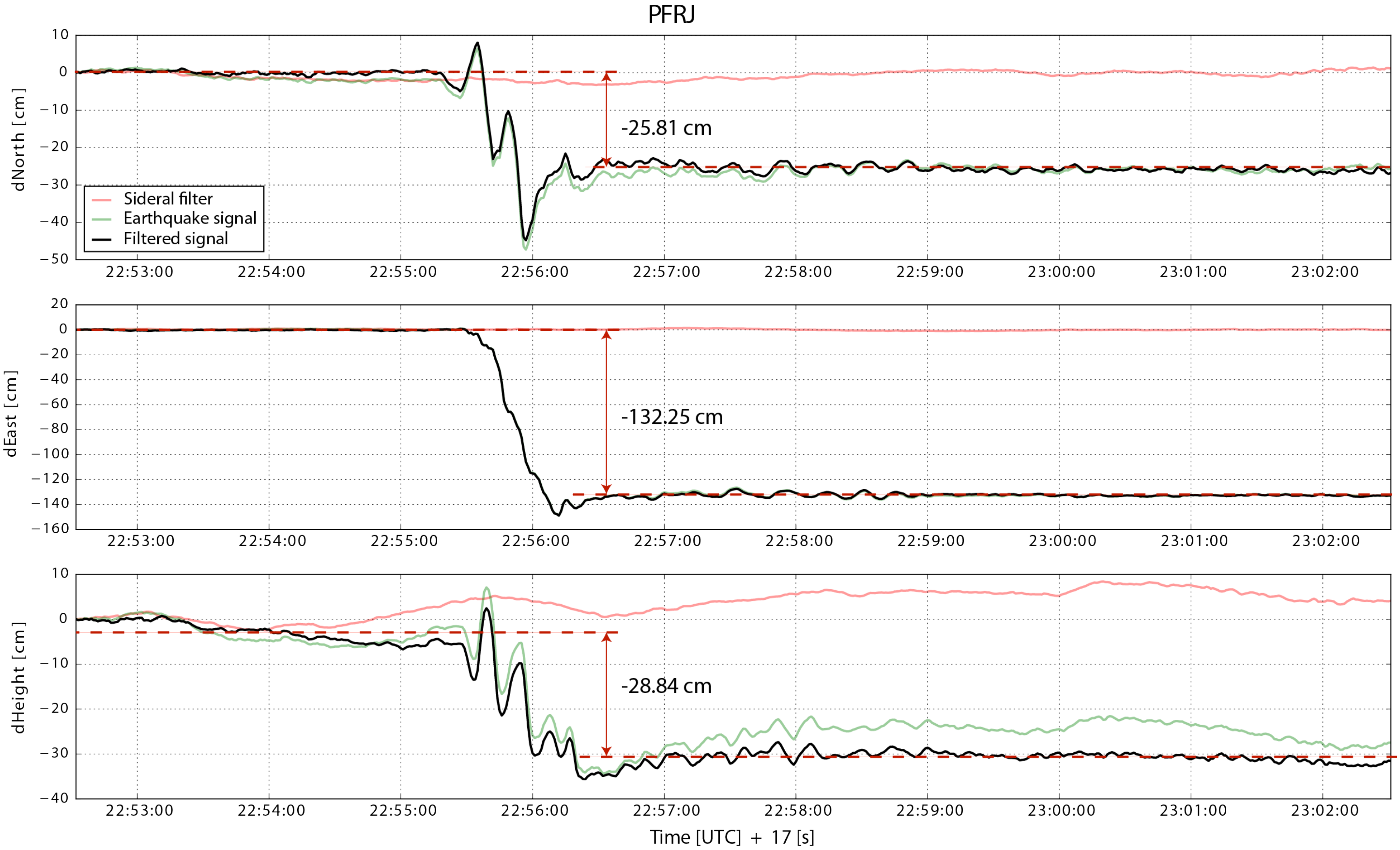

Figure S1 : Motogram of station Parque Frey Jorge (PFRJ) : green curve : original signal, red curve : sideral filter, black curve : filtered signal. The red arrows shows the estimation of static coseismic offset on the filtered motogram

Static GPS processing. 24 hr sessions are reduced to daily site positions using the GAMIT software [King & Bock 2000]. We choose the ionosphere-free combination , with fixed ambiguities to integer values. Precise orbits from the International GNSS Service for Geodynamics [IGS; Dow et al. 2009] are used together with the description from IGS tables of the phase centres of the antennae. We estimate one tropospheric vertical delay parameter per station every 3 hr. The horizontal (resp. vertical) components of the calculated relative position vectors have repeatabilities of 1–3 (resp. 3–5) mm. Daily time-series are then produced using the GLOBK software [Herring et al. 2010]. In order to deal with the large scale postseismic deformation following the Maule earthquae [Klein et al., 2016], we combine our daily solutions with daily global H-files produced at

SOPAC, using globally distributed IGS stations. We produce daily coordinates, mapped into the ITRF 2008 (Altamimi et al. 2011) using a set of regional and global stations with well-known coordinates in the ITRF08 [the reference frame can be found in Klein et al., 2016]. Residuals are typically of the order of 3–5 mm, indicating the level of precision of the mapping in the ITRF.

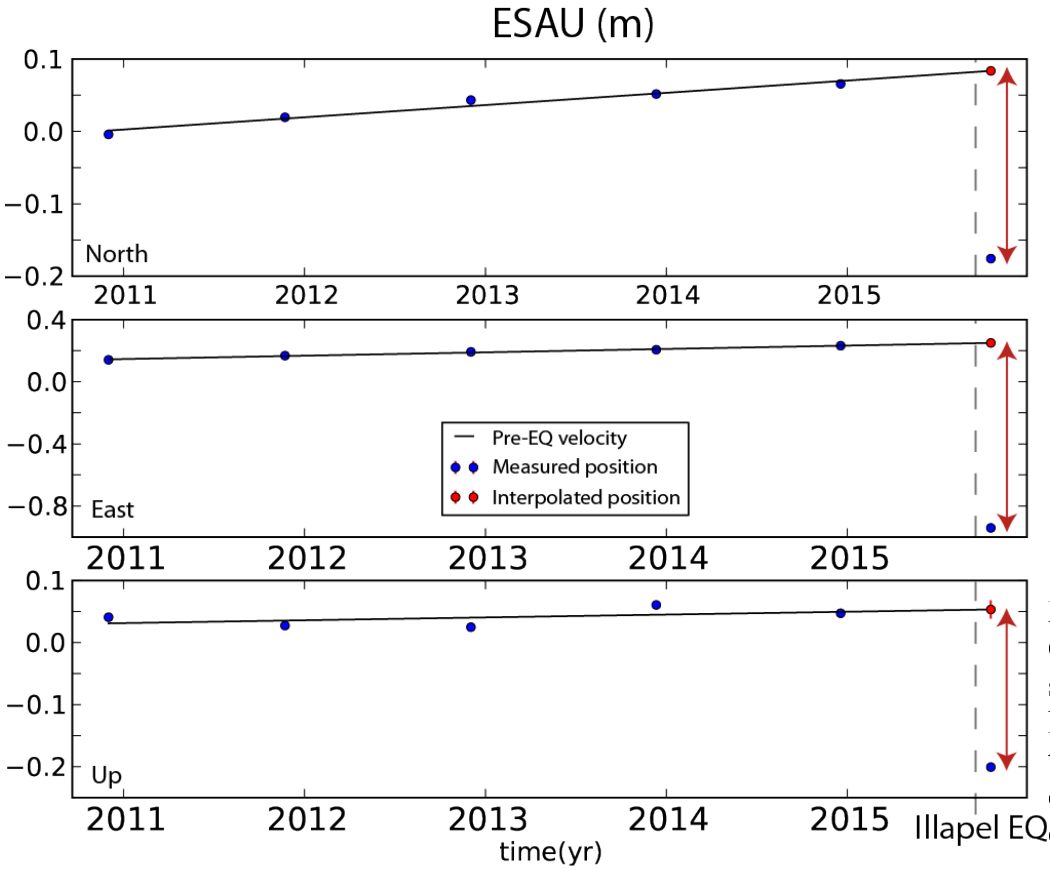

Figure S2 : Campaign time series of the site ESAU showing the process of coseismic estimation

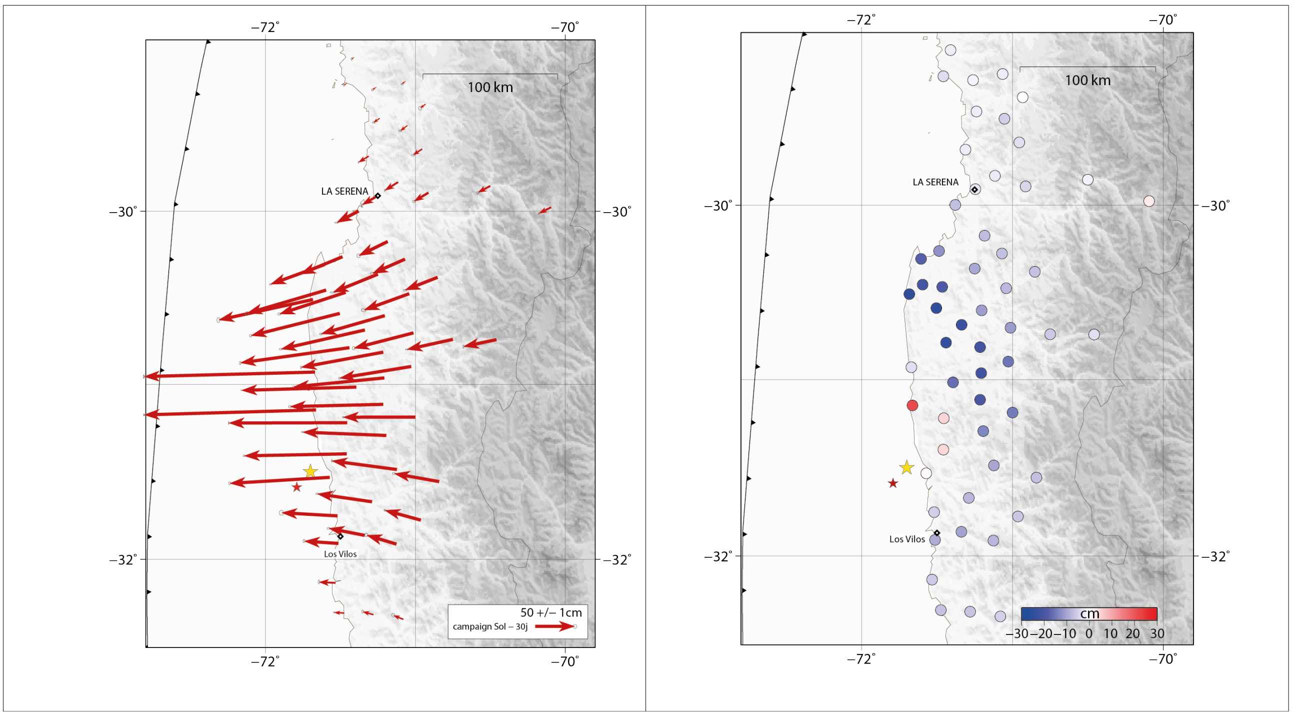

Fig. S3 : Co-seismic static displacement field for survey sites (at +15 to 30 days after the earthquake) on the horizontal (left) and vertical (right) components. Ellipses depict the 95% confidence level of formal uncertainties. The yellow star highlights the main shock epicenter, the red one, the strongest aftershock (CSN).

sGPS uncertainties estimation. The uncertainties are defined as $\sigma_{co}=\sqrt{\sigma_{extP}^{2}+\sigma_{inter}^{2}}$ (1)

with σ_{extP} the uncertainty on the post-earthquake position, and σ_{inter} defined as

$$\sigma_{inter}=\sqrt{\frac{\sum(\tilde{x}_i-x_i)^2}{n}} \quad (2)$$

where x_i are the campaign positions before the earthquake on which the interseismic velocity is interpolated, $\tilde{x}_i$ the positions predicted at the campaign date by the estimated interseismic velocity, and n the number of measurements used to estimate the interseismic velocity (fig.S2).

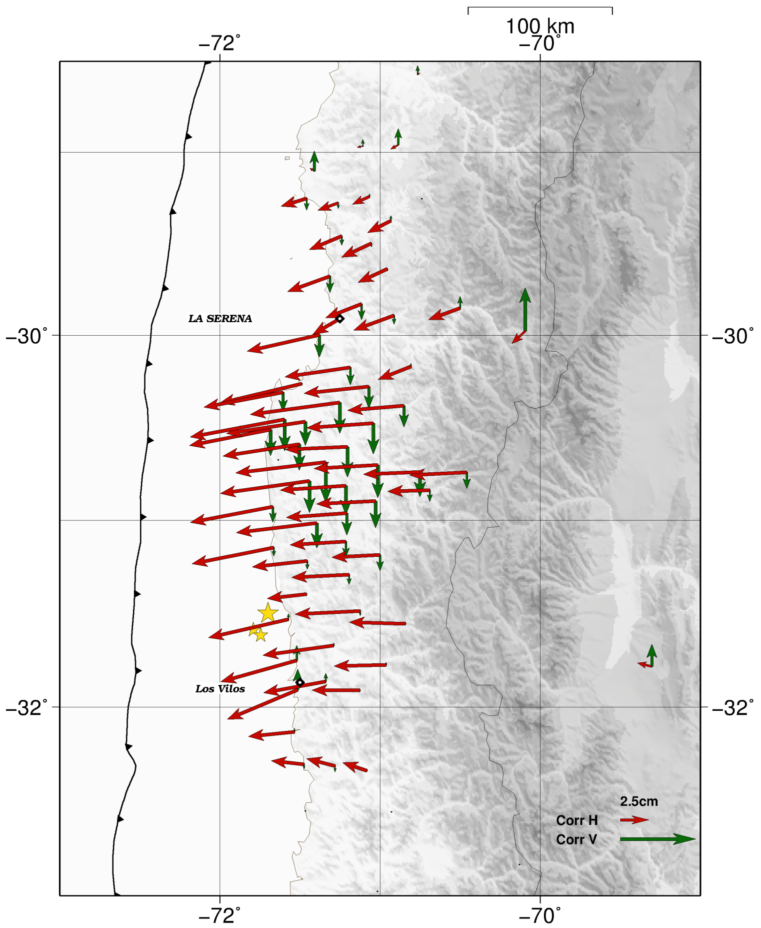

Figure S4 : Correction applied on survey sites horizontal (red arrows), and vertical (green arrows) to extract the purely coseismic deformation.

Note that vertical displacements measured by GPS are affected by a very large scale signal that has probably not a tectonic origin, producing 8mm of uplift on the whole network during the considered period. Therefore raw measurements are corrected from this drift fixing a null vertical displacement to the furthest stations considered.

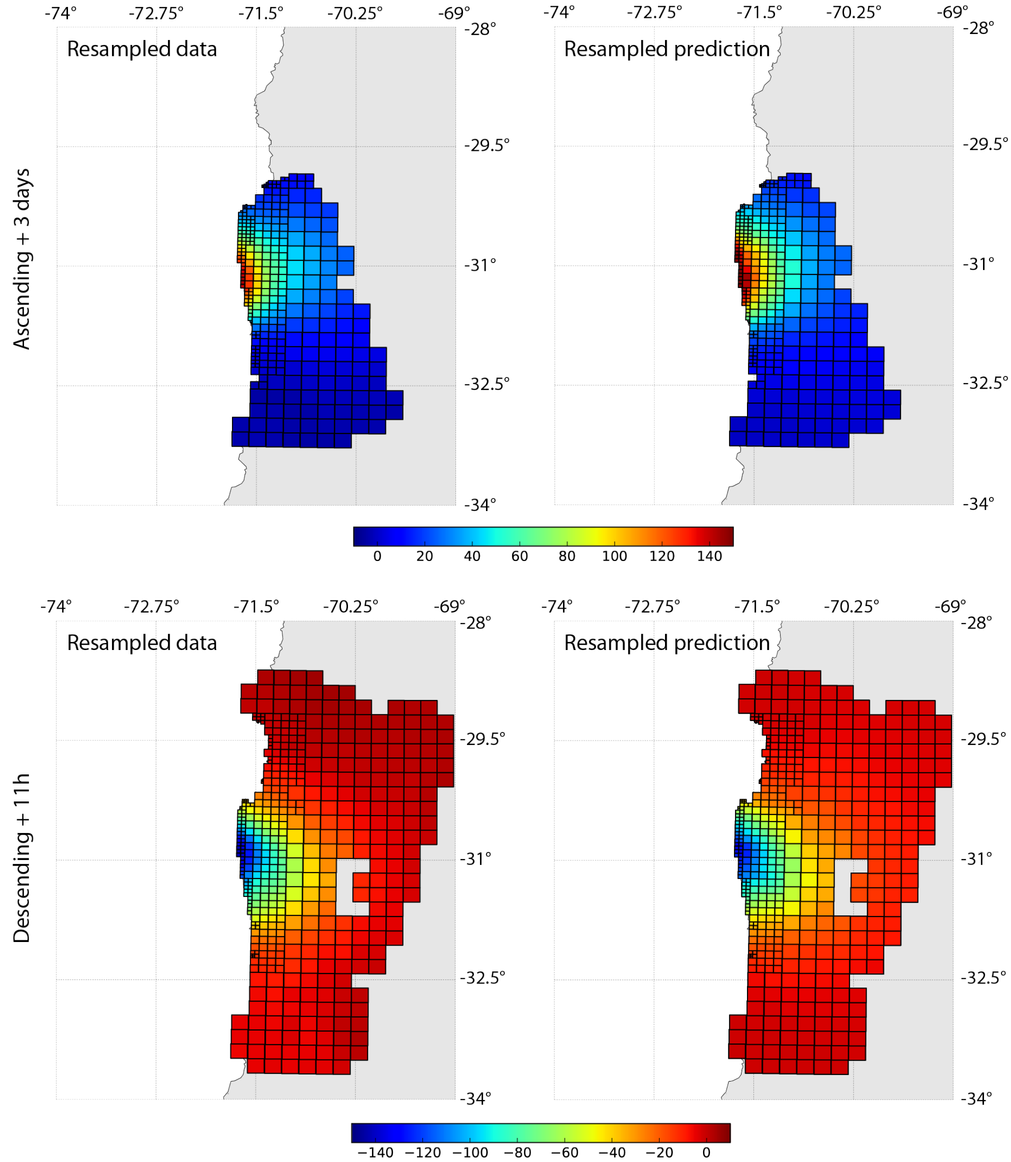

Fig. S5 Resampled INSAR interferograms for ascending and descending tracks vs interferograms predicted by the preferred model.

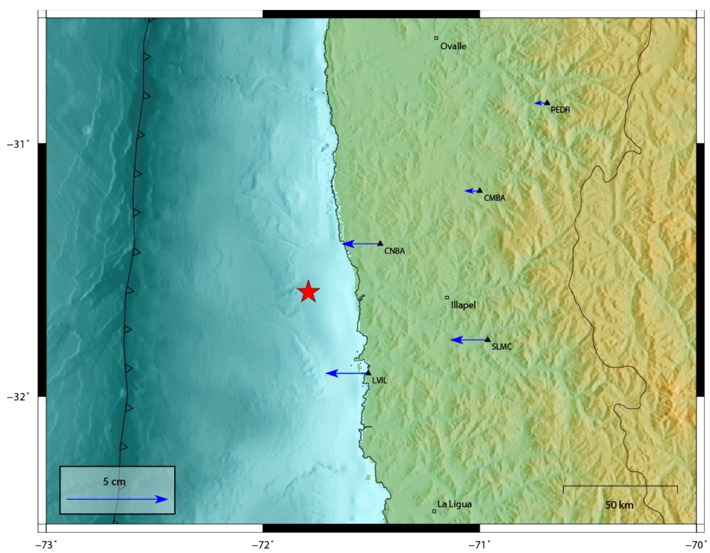

Fig S6a: Static coseismic displacement field of the main aftershock on the East component (in cm). The red star depicts the location of the epicenter.

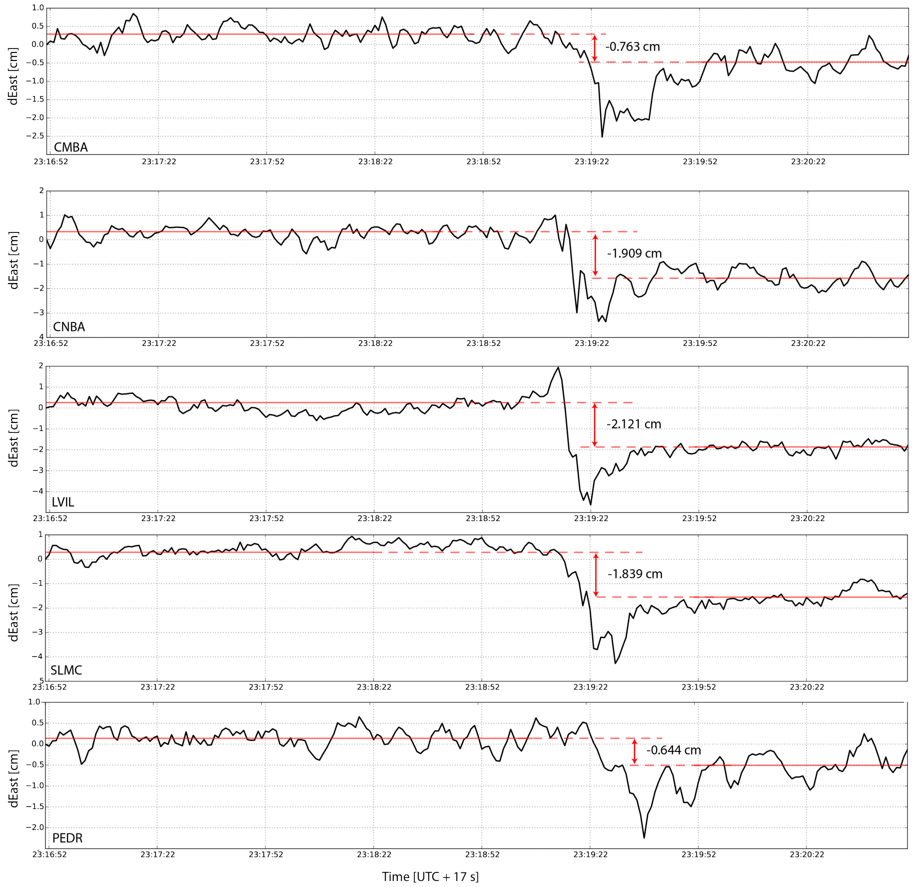

Fig S6b: Motograms (East component) of the 5 cGPS stations that recorded the main aftershock, used to estimate the static offset (Fig S6a).

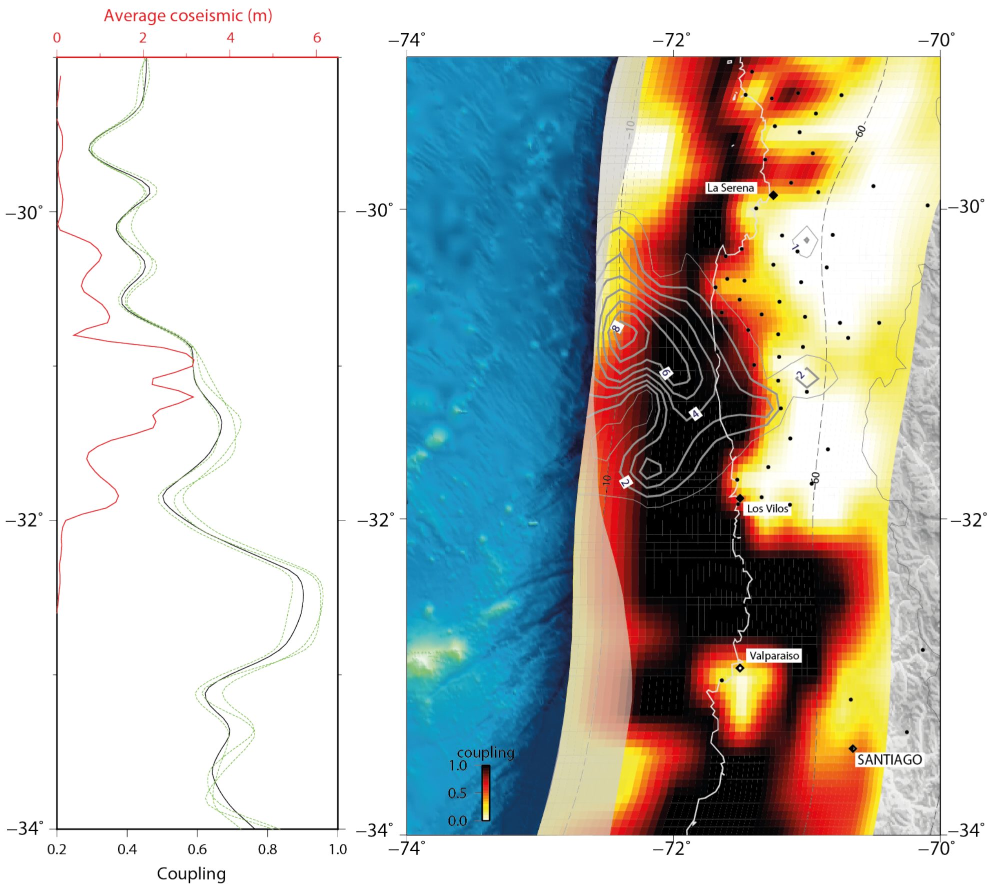

Fig. S7: Average coseismic slip amount for the best model (red curve also represented with grey 1m contours on the map) compared to along-strike variations of the average coupling value from the trench to 60 km depth (black curve, also represented on the map) and three alternative models that fit almost equally well with the data (different smoothing parameters, green dashed curves) [Métois et al., 2016].

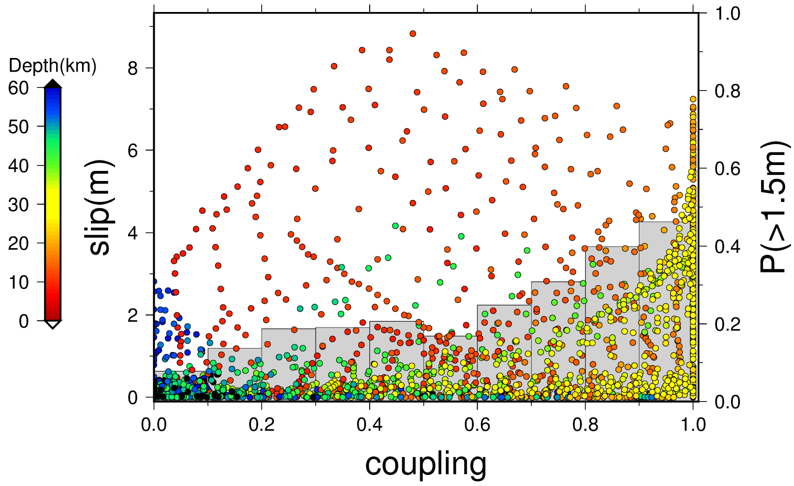

Fig. S8: Correlation between coseismic slip amount from the best model presented in fig. 4 and prevailing interseismic coupling from [Métois et al., 2016]. Each subfault is represented by dots color coded depending on its depth, coseismic slip during the Illapel earthquake and interseismic coupling value. Overall, the amount of coseismic slip is higher for higher coupling values. Outsiders to this tendency are mainly very shallow subfaults where resolution is low. The conditional probability of experiencing more than 1.5m of coseismic slip depending on the prevailing coupling amount is represented by gray histograms. The correlation coefficient R2 between P(>1.5m)/phi and the interseismic coupling is of 0.87.

Damping effect

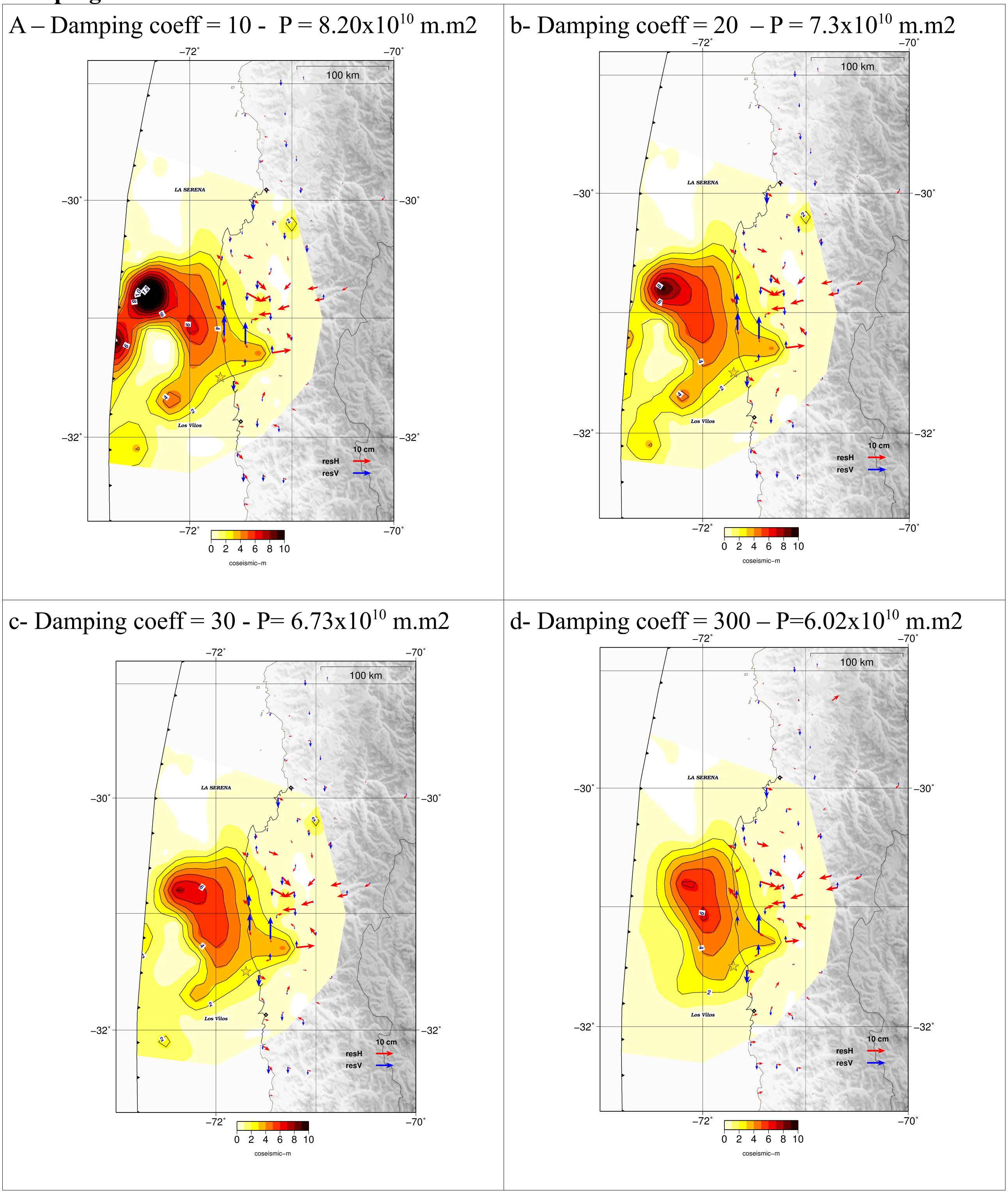

Fig.S9: Residuals (Observations – model, red arrow for the horizontal component and blue arrows for the vertical component) for models inverted using different damping values (A) 10, B) 20, C) 30, D) 300) corresponding to an increasing importance of the damping in the penalty function as described in table 1 in the main text. Rake angle is left free. The corresponding coseismic slip distribution is represented in red color scale. The potency (geometrical moment) is given in each case.

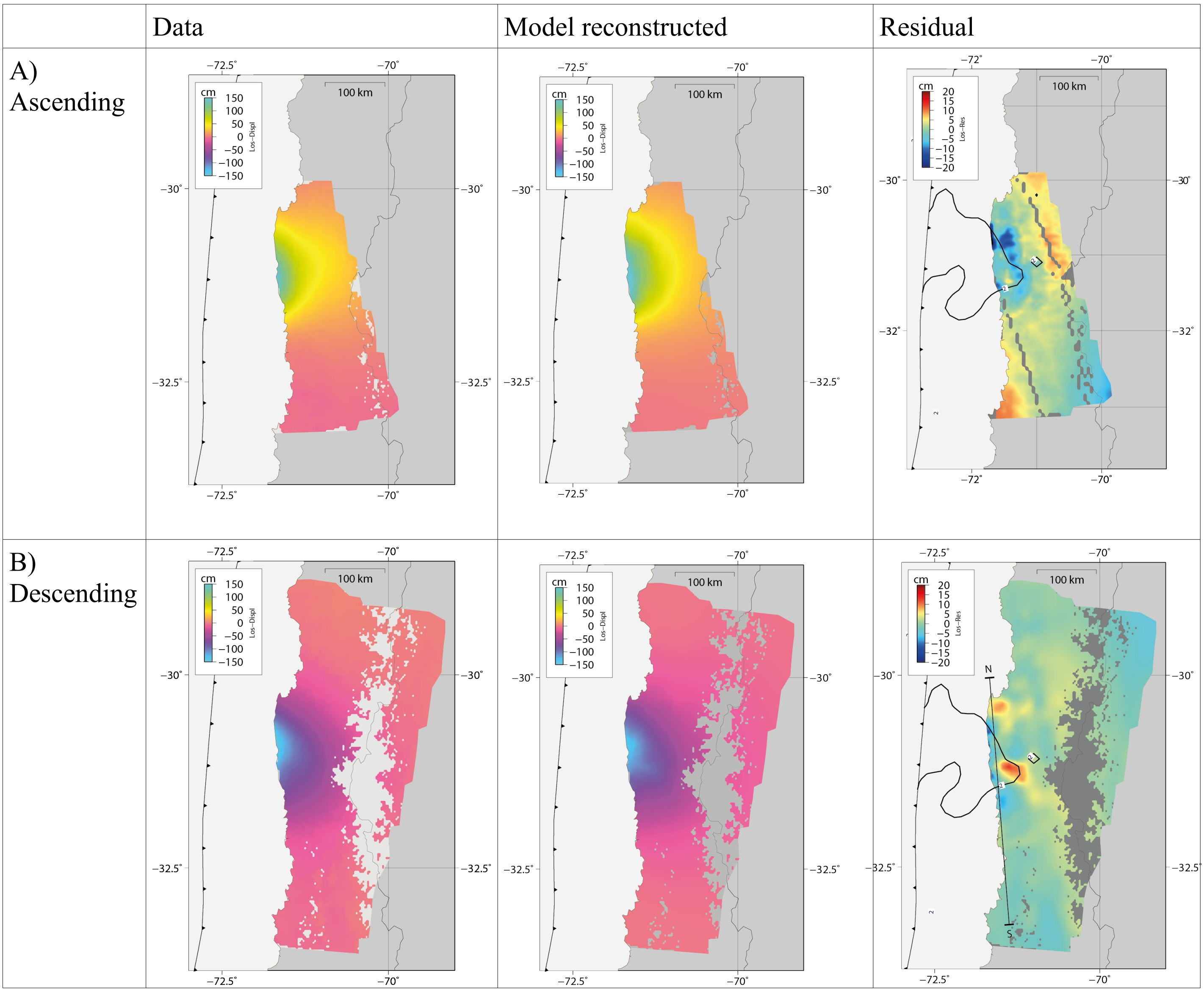

Fig. S10: Reconstructed unwrapped InSAR tracks (A) ascending and B) descending), prediction of the best fit model and residuals (observations – model)

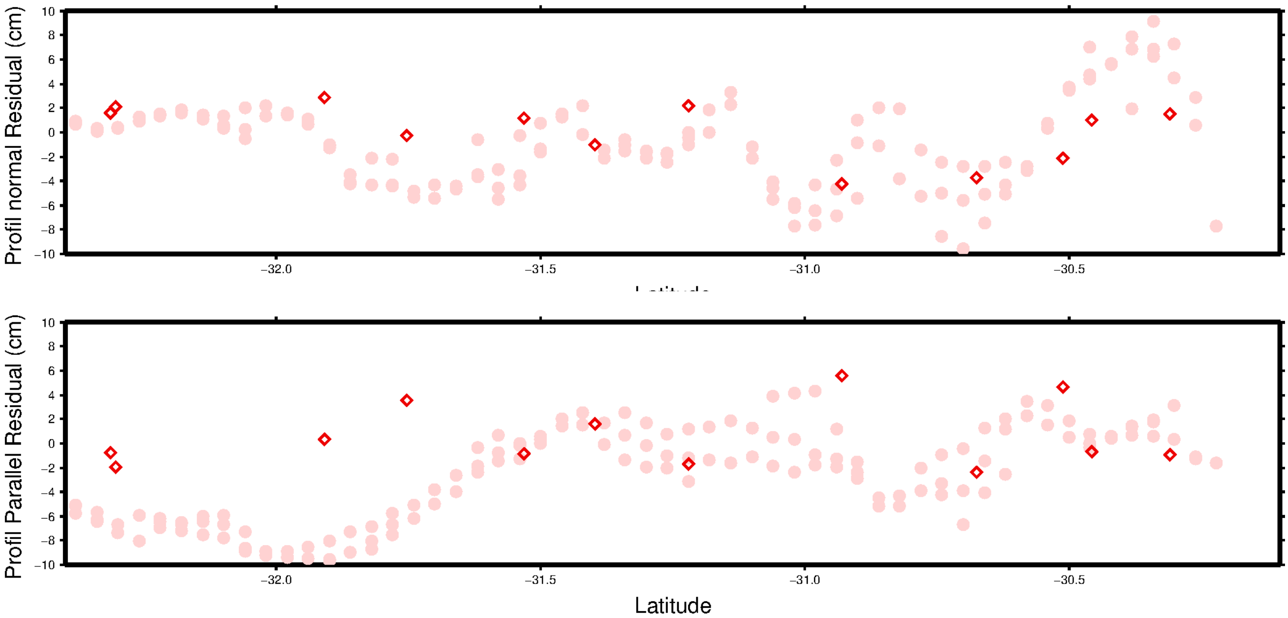

Fig. S11 : Profil-normal and profil-parallel residuals of InSAR (pink dots) and GPS (red diamonds) residuals (obs – mod) of the preferred best fit model along a North-South profile (represented on fig.S5B-residuals)

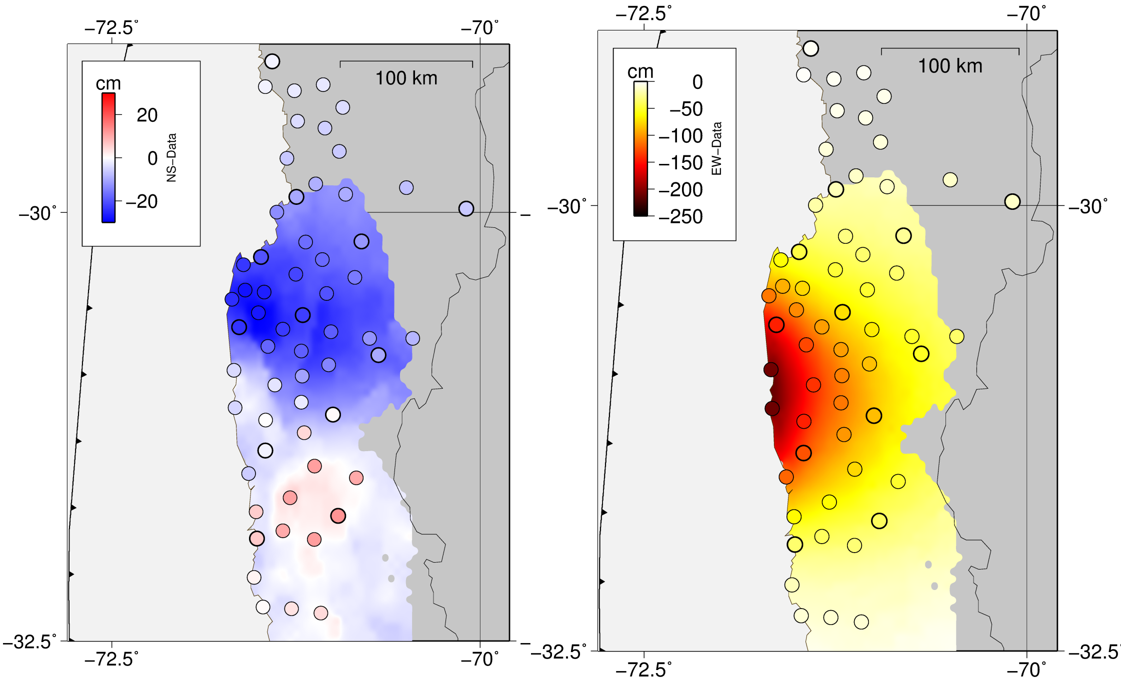

Fig. S12 : Horizontal coseismic displacements NS (left), EW (right) reconstructed from Sentinel-1 InSAR [Grandin et al.,2016] compared to GPS coseismic offsets. cGPS stations are depicted by darker contours.

.

Fig S13: **[HR solution – daily solution]** Slip distribution of the best fit model of the difference between the high rate and the daily coseismic static solutions corresponding to the main aftershock (epicenter depicted by the yellow star, CSN) plus postseismic deformation on the first hours after the main shock and the aftershock.
Estimated Mo = 2.14e20 N.m (Mw = 7.5)

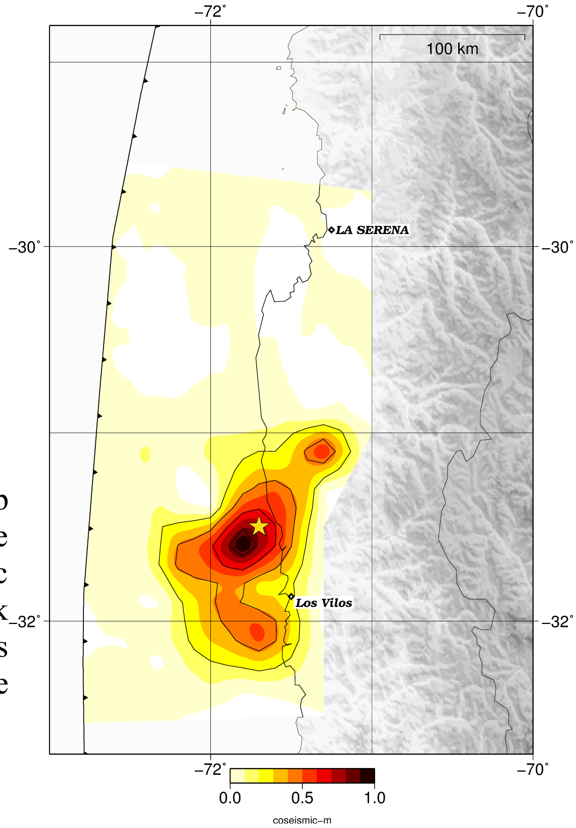

Moment estimation and seismic moment vs geodetic moment comparisons. With heterogeneous elastic parameters on both sides of the fault plane (our case), the calculation of the seismic moment is not as direct as in an homogeneous half space (most previous studies). We follow here two different methodologies to estimate a seismic moment that can be compared with other studies. The first method is 3-steps: First, we estimate the potency distribution, which is independent of the geometry. Then, this potency distribution is re-injected in a PREM distribution, homogeneous on both sides of the fault. And finally, we estimate the seismic moment in this PREM distribution, which makes it comparable with seismological studies. The second method is more straightforward: we compute the seismic moment using an effective shear modulus defined following [Wu & Chen, 2003] and [Vavrycuk et al., 2013] by :

$$\mu' = 2 \left(\mu^{+}.\mu^{-} / (\mu^{+} + \mu^{-})\right) \qquad (4)$$

Seismic moments calculated using both methodologies are very close (within 10%) (Table S1). Allowing the slip vector to vary or constraining it to the plate convergence direction does not change the seismic moment significantly either. The largest variations depend on the damping factor: almost 30% between the lowest and the highest estimates. Note that a contribution of some 2.0×10^{20}N.m., corresponding to earthquakes and slip during the first day should be added to the seismological estimate before comparison with the values from table 2. All are in the range of the seismological estimate.

	Damping variation	P (m.m2)	'Effective' distribution Mo (N.m)	'Effective' distribution Mw	PREM distribution Mo (N.m)	PREM distribution Mw
free rake	**cm10**	8.20E+010	3.56E+021	8.30	3.55E+021	8.30
	cm20	7.31E+010	3.24E+021	8.27	3.35E+021	8.28
	cm30	6.73E+010	3.04E+021	8.26	3.25E+021	8.27
	cm300	6.02E+010	2.80E+021	8.23	3.09E+021	8.26
fixed rake	**cm20**	8.25E+010	3.58E+021	8.30	3.53E+021	8.30
	Preferred mod (cm30)	7.68E+010	**3.38E+021**	8.29	**3.42E+021**	8.29

Table S1: Potency, Seismic moment and Magnitude estimated with the 2 methodologies, for 6 models with different damping value, with rake 'fixed' or 'free', to be compared with W-phase estimation: Mo = 3.19 x10^{21} N.m (Mw8.3) and Global CMT estimation : Mo=3.23x10^{21} N.m (Mw8.3).

Shallow slip or not - Sensitivity study

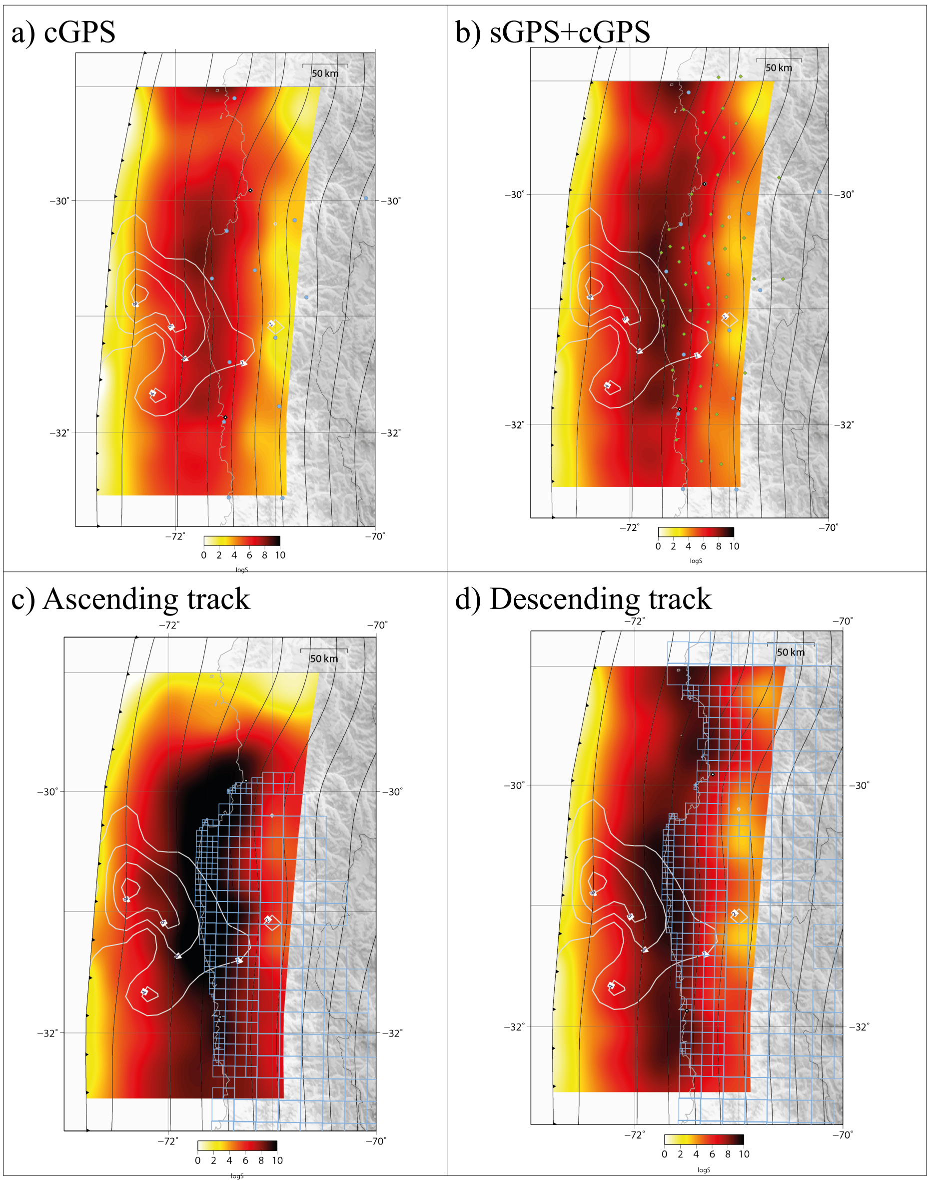

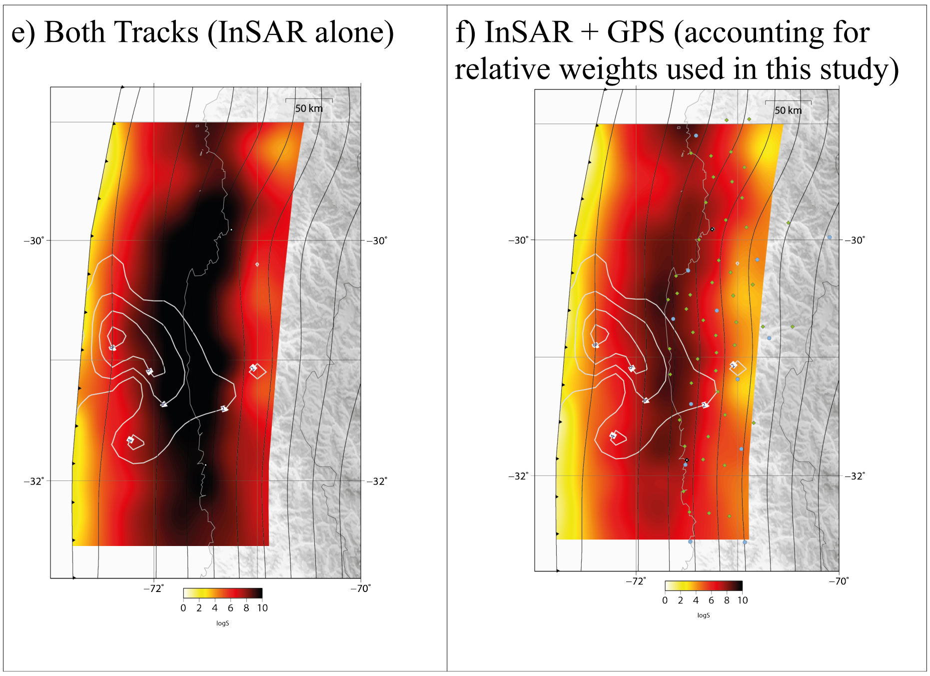

Fig.S14: Sensitivity (defined in equation (1)) maps for different datasets. **a)** cGPS only ; **b)** cGPS + sGPS ; **c)** InSAR ascending ; **d)** InSAR descending ; **e)** Two InSAR tracks ; **f)** cGPS+ sGPS + InSAR. Blue dots represent continuous GPS stations, green diamons campaigns sites, blue square contours represent resampled squares of InSAR. The 2m contours of the preferred coseismic model are represented in white. The 10 km-isolines from Slab1.0 are represented in black.

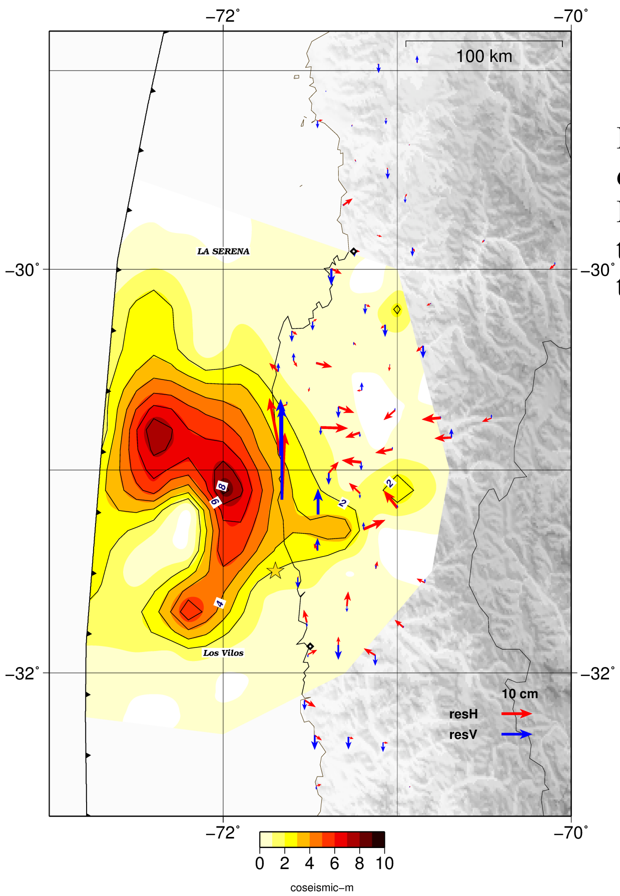

Fig.S15: Inverted coseismic slip distribution downweighting (ie eliminating them) the stations EMAT and CTAL located at the coast which have the maximum horizontal offsets. Arrows represent the residuals (red in horizontal, blue in vertical)

Geometry effect. The exact elastic moduli in the overriding and subducting plates and the thickness of the crust are poorly known, in particular on the shallowest part of the subduction interface. Seismic refraction studies have been conducted in North Chile (CINCA experiment) and in South Chile, focused on the Arauco Peninsula (SPOC experiment), but not in the region of the Illapel earthquake. There, a transition between erosive and accretionnary regime is proposed, supposedly due to morphologic changes of the oceanic plate [Oncken et al., 2006]. But precise evidences are sparse and the value of shear moduli remains unconstrained. Moreover, models of coseismic displacements very often involve a layered structure with similar crusts for the oceanic and continental crusts. Here, we simply test the impact of different geometries and elastic moduli of the subducting and overridding plates. In these tests, the damping coefficient is fixed to 100 and the rake angle is left free, so that geometry is the only varying parameter. We compare the slip distributions inverted with a 30 km thick continental crust and no oceanic crust (our preferred model – figS16-a); with a 40 km thick continental crust and no oceanic crust (fig.S16-b) and with equal parameters (30km - thick crust) on both sides of the fault (fig S16-c). The slip amplitude varies and is the strongest in the case of the homogeneous geometry, as expected: the artificial low moduli in the oceanic lithosphere favor stronger displacements below the subduction interface. Slip amplitude is also slightly stronger in the case of the 30 km-thick continental crust. We note that the potencies differ by 19% and the Mo by 14% between the case with a 40km thick crust (b) and the case with equal parameters on both sides (c) (table S2 in the supplementary material). This has to be compared with the spread of potencies and moments in table 2 which is similar. One should thus keep in mind that differences below 20% between the seismic moment deduced from seismology or from GPS and InSAR displacements could be due to errors in the elastic structure as well as to an inappropriate choice of the regularization parameters in the inversion. Note also that the widespread choice of a layered structure for the modeling of coseismic displacements significantly enhances the predicted moment.

	Case	Potency (m.m2)	Mo (PREM) (N.m)
a)	Crust 30 km	$8.63x10^{10}$	$4.0831x10^{21}$
b)	Crust 40 km	$7.97x10^{10}$	$3.844x10^{21}$
c)	Uniform Crust	$9.51x10^{10}$	$4.3961x10^{21}$

Table S2 : Estimated potencies and seismic moment for each models.

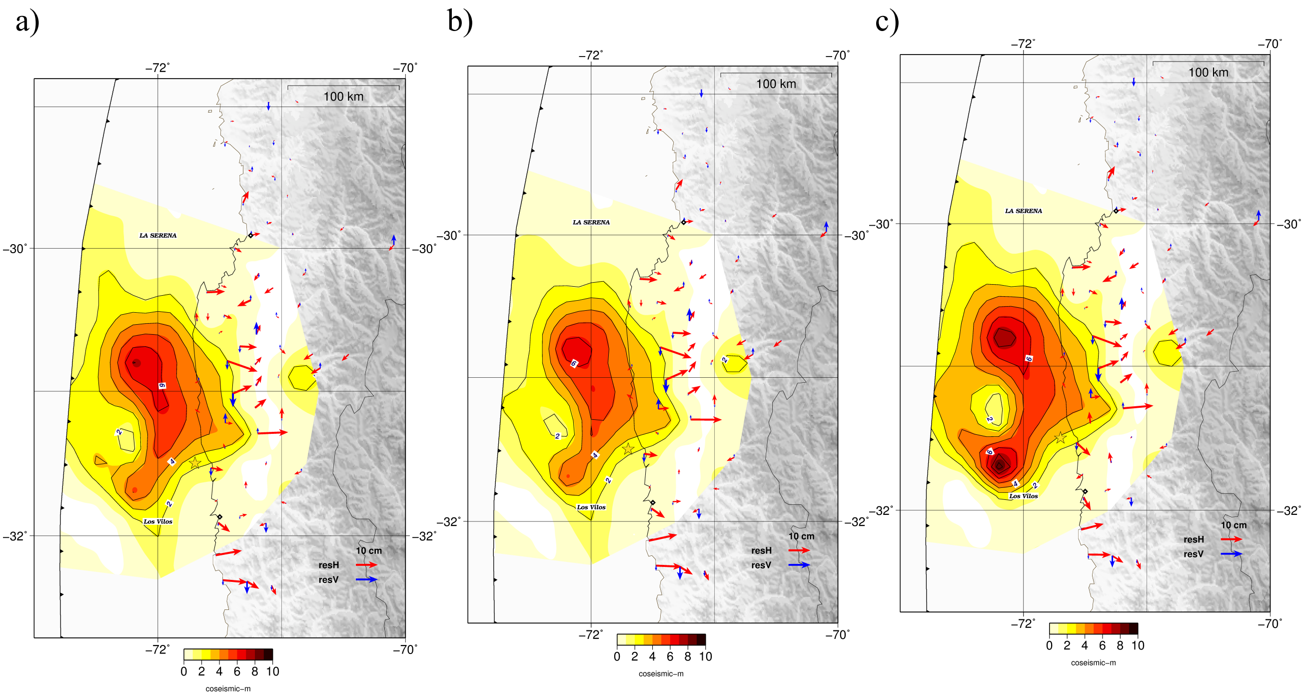

Fig.S16: Effect of crust on coseismic slip distribution :
a) standard crust (continental crust 30km – thick, no oceanic crust) ; b) thicker crust (continental crust 40 km – thick, no oceanic crust) ; c) uniform geometry (30-thick crust on both oceanic and continental crust). In the 3 cases, inversions are made with GPS data only, with rake 'free' and damping of 100. Arrows represent the residuals (red in horizontal, blue in vertical)

References

Altamimi, Z., Collilieux, X., & Métivier, L. (2011). ITRF2008: an improved solution of the international terrestrial reference frame. *Journal of Geodesy*, *85*(8), 457-473.

J. Dow, R. Neilan, C. Rizos, The International GNSS Service in a changing landscape of Global Navigation Satellite Systems, Journal of Geodesy 83 (3- 4) (2009) 191–198. doi:10.1007/s00190-008-0300-3.

Grandin, R., Klein, E., Métois, M., & Vigny, C. (2016). Three-dimensional displacement field of the 2015 Mw8. 3 Illapel earthquake (Chile) from across-and along-track Sentinel-1 TOPS interferometry. *Geophysical Research Letters*, *43*(6), 2552-2561.

Herring, T., King, R., and McClusky, S. C. (2010). GLOBK : Global Kalman filter VLBI and GPS analysis program release 10.4.

R. King, Y. Bock, Documentation for the GAMIT Analysis Software, release 10.0, 2000.

Klein, E., Fleitout, L., Vigny, C., & Garaud, J. D. (2016). Afterslip and viscoelastic relaxation model inferred from the large-scale post-seismic deformation following the 2010 Mw 8.8 Maule earthquake (Chile). *Geophysical Journal International*, *205*(3), 1455-1472.

Métois, M., Vigny, C., & Socquet, A. (2016). Interseismic Coupling, Megathrust Earthquakes and Seismic Swarms Along the Chilean Subduction Zone (38°–18° S). *Pure and Applied Geophysics*, *173*(5), 1431-1449.

Oncken, O., Chong, G., Franz, G., Giese, P., Götze, H.-J., Ramos, V. A., Strecker, M. R., and Wigger, P. (2006). The Andes : active subduction orogeny. Springer Science & Business Media.

Vavryčuk, V. (2013). Is the seismic moment tensor ambiguous at a material interface?. *Geophysical Journal International*, *194*(1), 395-400.

Wu, Z. L., & Chen, Y. T. (2003). Definition of seismic moment at a discontinuity interface. *Bulletin of the Seismological Society of America*, *93*(4), 1832-1834.